

Towards multifocal ultrasonic neural stimulation: pattern generation algorithms

Yoni Hertzberg^{1,2,*}, Omer Naor^{3,*}, Alexander Volovick¹ and Shy Shoham^{4,5}

¹ InSightec LTD, Tirat Carmel, Israel

² Department of Physics, Tel-Aviv University, Israel

³ The Interdisciplinary Centre for Neural Computation, The Hebrew University of Jerusalem, Edmond J. Safra Campus, Givat Ram, Jerusalem 91904, Israel

⁴ Faculty of Biomedical Engineering, Technion-Israel Institute of Technology, Israel

E-mail: sshoham@bm.technion.ac.il

Received 17 February 2010


Accepted for publication 1 July 2010

Published 18 August 2010

Online at stacks.iop.org/JNE/7/056002

Abstract

Focused ultrasound (FUS) waves directed onto neural structures have been shown to dynamically modulate neural activity and excitability, opening up a range of possible systems and applications where the non-invasiveness, safety, mm-range resolution and other characteristics of FUS are advantageous. As in other neuro-stimulation and modulation modalities, the highly distributed and parallel nature of neural systems and neural information processing call for the development of appropriately patterned stimulation strategies which could simultaneously address multiple sites in flexible patterns. Here, we study the generation of sparse multi-focal ultrasonic distributions using phase-only modulation in ultrasonic phased arrays. We analyse the relative performance of an existing algorithm for generating multifocal ultrasonic distributions and new algorithms that we adapt from the field of optical digital holography, and find that generally the weighted Gerchberg–Saxton algorithm leads to overall superior efficiency and uniformity in the focal spots, without significantly increasing the computational burden. By combining phased-array FUS and magnetic-resonance thermometry we experimentally demonstrate the simultaneous generation of tightly focused multifocal distributions in a tissue phantom, a first step towards *patterned* FUS neuro-modulation systems and devices.

 Online supplementary data available from stacks.iop.org/JNE/7/056002/mmedia

(Some figures in this article are in colour only in the electronic version)

1. Introduction

Ultrasonic phased arrays are widely used in focused ultrasound (FUS) systems and applications where their ability to generate a tight, intense and electronically steerable focal region from a distributed source is desirable. Another potential (but yet unexploited) advantage of ultrasonic phased arrays in

biomedicine is their ability to generate fields with multiple *simultaneous* foci or spatially extended focal regions. In the context of hyperthermia treatments, for example, it has been suggested that multi-focal ultrasound distributions would result in a more uniform temperature field, which could be more finely controlled and quicker to create [1–3]. In ultrasonic neuro-modulation, an emerging application of FUS [4–9], multi-focal ultrasonic distributions may also be used for patterned simultaneous stimulation, inhibition or modulation

⁵ Author to whom any correspondence should be addressed.

* Equal contribution by these authors.

of neural structures and populations, such as multi-focal light distributions are already being applied for parallel photo-stimulation [10–13]. In contrast to visible light, FUS is not heavily scattered or absorbed when penetrating biological tissues and may be applied completely non-invasively to various neural structures including cortical areas and even deep-seated nuclei [9].

In this paper, we introduce and study new algorithms for the phased-array generation of *ultrasonic* multi-focal distributions by adapting algorithms previously developed for the generation of *optical* computer-generated holograms (CGH) using a spatial light modulator (SLM). Computer-generated digital holography is a relatively mature framework where many algorithms have already been developed and studied for their relative performance characteristics [14–16]. Interestingly, we note that there is an underlying similarity between methods developed for controlling optical SLMs, and the few methods previously developed for generating multiple *ultrasonic* foci, such as Ibinni *et al*'s 'conjugate field method' [1] and Ebbini *et al*'s 'pseudo-inverse method' [2, 17, 18]. Many SLMs are phase-only, and can physically only manipulate the phase of the incoming optical wave, while maintaining uniform amplitude. Similarly, although many ultrasonic phased arrays can control both the phase and the amplitude of the generated wavefront, it is generally desirable to use the full power capacity (maximal amplitude) of each transducer. This has motivated Ebbini *et al* to introduce a second computational stage aimed at forcing a solution in which the elements' amplitudes are more uniform, leading indirectly to the same sort of solutions.

This paper describes the application of modified CGH algorithms to create multiple ultrasonic foci. The computation of a simulated ultrasonic field generated by a phased-array source is described in section 2. The pseudo-inverse and selected CGH algorithms are formulated in section 3, as well as a description of the experimental setup used to generate US patterns and measure the results via MR-thermometry. Section 3.2 reports the simulation and experimental results, and section 4 discusses these results and their significance, limitations and future prospects. Detailed mathematical derivations of the algorithms are available as supplementary data at stacks.iop.org/JNE/7/056002/mmedia.

2. Theory and simulations

The pressure at point r is related to the particle velocity normal to the source's surface by the Rayleigh–Sommerfeld integral over the source's surface:

$$p(r) = \frac{j\rho ck}{2\pi} \int u(r') \frac{\exp(-jk d_{rr'})}{d_{rr'}} dS \quad (1)$$

where ρ is the medium's density, c is the velocity of sound in the medium, k is the wave number, $u(r') = |u(r')| e^{j\varphi_{r'}}$ is the complex velocity at point r' on the source's surface and $d_{rr'}$ is the distance between r and r' . To compute the complex pressure created by a phased array with N elements, we make the simplifying assumption that each phased-array element produces a spherical wavefront emanating from an imaginary point source at the centre of the element, with an amplitude

proportional to the elements' area S_{el} . Collecting constants into a single constant $K = \frac{\rho ck}{2\pi} S_{el}$ and the complex pressure at r_m , the location of the m th target ($m = 1, \dots, M$) becomes

$$p(r_m) = jK \sum_n d_{mn}^{-1} |u_n| \exp(j\varphi_n) \exp(-jk d_{mn}). \quad (2)$$

Here d_{mn} is the distance between the centre of the n th element and the m th target. This equation may also be written in matrix notation [2]:

$$\underline{p} = H \underline{u}, \quad (3)$$

where the relation between the excitation of the n th element and the pressure at the m th target is given by $H(m, n) = jK d_{mn}^{-1} \exp(-jk d_{mn})$, \underline{u} is the $N \times 1$ excitation vector $u_n = |u_n| \exp(j\varphi_n)$ and \underline{p} is the $M \times 1$ vector describing the pressure's complex amplitude at each target. The ultrasonic intensity at the target is given by $I_m = \frac{|p(r_m)|^2}{2\rho c}$. A single, high-intensity focus is obtained by setting each element's phase to $\varphi_n = k d_{1n}$ and all elements' amplitudes to the maximum $U = |u|_{\max}$, which results in $p(r_1) = jK U \sum_n d_{1n}^{-1}$ and $I_1 = \frac{(K U \sum_n d_{1n}^{-1})^2}{2\rho c}$ which is the maximum intensity deliverable to a single point at the same distance from the array.

In the context of optical waves it is common and beneficial to formulate 'Fresnel's approximation' of equation (2) [19], in which the distance between two points is simplified. The expression for the distance is $d_{mn} = \sqrt{(x_m - x_n)^2 + (y_m - y_n)^2 + z^2} = z \sqrt{1 + \frac{(x_m - x_n)^2}{z^2} + \frac{(y_m - y_n)^2}{z^2}}$ and after a first-order binomial expansion $d_{mn} \approx z [1 + \frac{1}{2} (\frac{x_m - x_n}{z})^2 + \frac{1}{2} (\frac{y_m - y_n}{z})^2]$. This expression replaces d_{mn} in the phase term of (2), while the zeroth-order expansion— z —is used for the amplitude term, so the approximated equation is

$$p(r_m) \approx jK z^{-1} \exp(-jkz) \sum_n |u_n| \exp(j\varphi_n) \times \exp \left\{ -j \frac{k}{2z} [(x_m - x_n)^2 + (y_m - y_n)^2] \right\}. \quad (4)$$

Note that for a phase-only phased array the excitation amplitude is constant, so the terms summed in (4) are all phase terms, which is important for the derivation of several CGH algorithms. This approximation is valid if the targets are in the array's intermediate near field or far field, i.e. if the axial distance z between the array and target planes is greater than $\frac{D^2}{4\lambda}$, where D is some characteristic diameter of the transducer [20]. This is a problematic assumption when dealing with multi-element arrays, which tend to be large, as the required target distance becomes too large for practical setups. We therefore choose a limited approximation, only approximating $d_{mn}^{-1} \approx z^{-1}$ in the amplitude expression, which is valid at shorter distances yet allows deriving a modified version of the algorithms as the terms summed in (4) are again only phase terms.

To simulate the field created by a phase-only phased array we use equation (2), requiring uniform velocity amplitudes. The simulations are based on the geometry and physical properties of the experimental planar phased array (see below), which operates with a central frequency of 2.3 MHz, has $N = 987$ elements with an area of 1 mm^2 , arranged over an aperture of $25 \times 40 \text{ mm}^2$. During the array's design

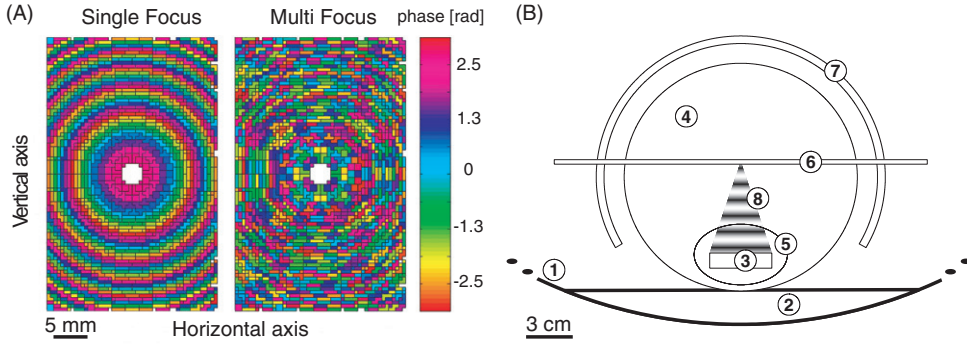


Figure 1. The transducer and experimental layout. (A) The simulated and experimental ultrasound phased-array transducer: structure and element phases. Left—phase map for producing a single focus 60 mm above the centre of the transducer. Right—phase map calculated using the GSW algorithm for nine foci. (B) A schematic illustration of the experimental layout. (1) Magnet bore (truncated), (2) MRI bed, (3) US transducer, (4) gel phantom, (5) degassed water, (6) image plane, (7) RF coil and (8) acoustic path.

and production, its elements' arrangement was chosen semi-randomly (see figure 1(A)) in order to reduce hot spots outside the focus region [17]. The simulated maps have a pixel size of $S = \frac{\lambda}{8} \times \frac{\lambda}{8} = (0.082)^2 \text{ mm}^2$.

3. Methods

3.1. Algorithms

There is no analytical solution to the problem of determining the phases which would generate an optimal intensity distribution. We implemented a number of algorithms for computing the required array phases, including the pseudo-inverse (PINV) algorithm [2], as well as several algorithms developed for computing CGH [14] including the random mask (RM), random superposition (SR), Gerchberg–Saxton (GS) and weighted Gerchberg–Saxton (GSW) algorithms. The algorithms are described below briefly and their derivations appear as supplementary data available at stacks.iop.org/JNE/7/056002/mmedia. The algorithms' performances in creating a pattern were quantified using two fundamental parameters.

- (a) *Normalized efficiency*: $e = \frac{1}{P_s} \sum_m P_m$, where $P_m \equiv S \cdot \sum_{l=1}^L I_{m,l}$ is an estimate of the power delivered to the m th target, computed over L pixels that cover the focal spot (each with an area S defined above) and P_s is the power delivered to a 'pattern' of a single focus (located at the centre of the target plane).
- (b) *Uniformity* of power delivery to the targets: $u = 1 - \frac{P_{\max} - P_{\min}}{P_{\max} + P_{\min}}$, where $P_{\max} = \max_m \{P_m\} = \max_m \{S \cdot \sum_{l=1}^L I_{m,l}\}$ and P_{\min} is defined in a similar fashion.

PINV: the pseudo-inverse algorithm's first step is the minimum norm solution of the matrix equation (3), which uses the pseudo-inverse of H : $\underline{u} = H^H (H H^H)^{-1} \underline{p}$, where H^H is the conjugate transpose of H . This solution ensures that the pressure is indeed as prescribed in \underline{p} at the chosen points in space, allowing good uniformity, and that $\|\underline{u}\|$ is minimal, not necessarily a beneficial feature in terms of efficiency. Therefore, the following iterations are aimed at

obtaining a solution with a more uniform excitation vector by introducing the weighting matrix W into the equation: $\underline{u} = W H^H (H W H^H)^{-1} \underline{p}$. W is initialized as $W^0 = I$ and its diagonal entries are updated with the rule $W_{nn}^t = |u_n^{t-1}|^{-1}$. When the algorithm converges at some step $t = \tau$, the phases of the result are used to drive the phased array:

$$\varphi_n^{\text{PINV}} = \arg\{[W^\tau H^H (H W^\tau H^H)^{-1} \underline{p}]_n\}. \quad (5)$$

In order to decide if the algorithm has converged or not, a relative change in the total power delivered to the targets,

$$\delta_p^t = \left| \frac{\sum_m P_m^t - \sum_m P_m^{t-1}}{\sum_m P_m^{t-1}} \right|, \quad (6)$$

is calculated at each iteration step, and the next iteration is initiated if the convergence condition $\delta^t < \delta^{\text{stop}}$ is not met. The choice of this convergence criterion for PINV facilitates the comparison with the CGH algorithms, yet note that in [2] the criterion was based on the uniformity of excitation vector's amplitudes. In our simulations the latter criterion increased at least twofold the number of iterations, but did not improve the efficiency or uniformity of power delivery to the targets.

For our multifocal patterns we defined the required pressure vector as $p_m \equiv 1$ in order to achieve a uniform pattern, although for non-uniform patterns it may be defined otherwise.

RM: this rudimentary algorithm randomly selects one of the targets— m for each element n —and sets $\varphi_n^{\text{RM}} = kd_{mn}$. Thus each element treats a single target as if it were the only focal point. In preliminary simulations we found this algorithm to behave quite poorly in terms of efficiency and uniformity and it was only used as an initializing step for the iterative algorithms.

SR: the following algorithms have physical optics interpretations but can also be formulated as solutions to optimization problems. The starting point is the assumption of uniform excitation amplitudes $u_n \equiv U$ and after the constant jKu is disregarded, a simplified expression for the applied field is obtained $\tilde{p}_m = \sum_n d_{mn}^{-1} \exp[j(\varphi_n - kd_{mn})]$.

The S algorithm maximizes the real part of the sum of complex amplitudes $\sum_m \text{Re}\{\tilde{p}_m\}$. We

require $\frac{\partial}{\partial \varphi_n} \sum_m \text{Re}\{\tilde{p}_m\} = 0$ and obtain $\varphi_n = \arg\left\{\sum_m d_{mn}^{-1} \exp(jkd_{mn})\right\}$. SR is an improved version that maximizes the pressure amplitudes projected on random directions in the complex plane, requiring $\frac{\partial}{\partial \varphi_n} \sum_m \text{Re}\{\tilde{p}_m \exp(-j\theta_m)\} = 0$ and obtaining

$$\varphi_n^{\text{SR}} = \arg\left\{\sum_m d_{mn}^{-1} \exp[j(kd_{mn} + \theta_m)]\right\}, \quad (7)$$

θ_m being the random variables uniformly distributed in $[0, 2\pi]$.

GS: here we apply the limited approximation described above and seek to maximize the sum of magnitudes delivered to the targets: $\sum_m |\tilde{p}_m| \approx z^{-1} \sum_m |\sum_n \exp[j(\varphi_n - kd_{mn})]|$. Now the distance z in the simplified expression for \tilde{p}_m is uniform and may be neglected as well in the optimization process, which results in the solution $\varphi_n^{\text{GS}} = \arg\left\{\sum_m \exp(jkd_{mn}) \frac{\tilde{p}_m}{|\tilde{p}_m|}\right\}$. As \tilde{p}_m is not known this is an implicit solution and is used as an iteration formula, in which the phases are initially determined by a simpler one-step algorithm (e.g. RM, SR), and at each iteration step the phases are computed according to the pressure field resulting from the previous step's phases:

$$\varphi_n^{\text{GS}}(t) = \arg\left\{\sum_m \exp(jkd_{mn}) \frac{p_m^{t-1}}{|p_m^{t-1}|}\right\}. \quad (8)$$

The criterion for convergence used here is identical to the PINV convergence criterion.

GSW: this extension to GS maximizes a similar weighted sum of magnitudes $\sum_m w_m |\tilde{p}_m|$, but under the constraint that all the target amplitudes are identical. This results in a weighted iteration formula:

$$\varphi_n^{\text{GSW}}(t) = \arg\left\{\sum_m w_m^t \exp(jkd_{mn}) \frac{p_m^{t-1}}{|p_m^{t-1}|}\right\}, \quad (9)$$

in which the weights are initialized as $w_m^0 \equiv 1$ and iterated as $w_m^t \equiv w_m^{t-1} \frac{(|p_m^{t-1}|)}{|p_m^{t-1}|}$. Intuitively, the weights normalize $|p_m|$ to the mean pressure reducing deviations from the mean. As this algorithm explicitly attempts to maximize efficiency and uniformity, we define the relative improvement in uniformity,

$$\delta_u^t = \left| \frac{u^t - u^{t-1}}{u^{t-1}} \right|, \quad u^t = 1 - \frac{P_{\max}^t - P_{\min}^t}{P_{\max}^t + P_{\min}^t}, \quad (10)$$

and the convergence condition examined at each iteration is $\delta^t = \max\{\delta_p^t, \delta_u^t\} < \delta^{\text{stop}}$.

It is possible to design a non-uniform field using the above CGH algorithms by weighting each target m in the relevant sum by an appropriate constant. For example, designing a non-uniform field using the GSW algorithm, equation (9) may be modified to

$$\varphi_n^{\text{GSW}}(t) = \arg\left\{\sum_m a_m w_m^t \exp(jkd_{mn}) \frac{p_m^{t-1}}{|p_m^{t-1}|}\right\}. \quad (11)$$

Selection of e.g. $a_k = 2a_l$ will result in a pressure amplitude at the k th target which is twice the amplitude at the l th target.

3.2. Experiments

The experiments were performed using Insightec's magnetic resonance guided FUS system, which integrates Insightec's ultrasound phased-array transducer and GE's 1.5T magnetic resonance imaging (MRI) system. The ultrasound phased array's arrangement is as described in the theory and simulations sections, except that it is limited to the transmission of eight phases, which span the 2π phase dimension. The transducer's aperture ($25 \times 40 \text{ mm}^2$), element area (1 mm^2) and central frequency (2.3 MHz) were similar to those assumed in the simulations. The acoustic energy was transmitted via degassed water to a tissue-mimicking gel phantom that wrapped the ultrasound transducer.

The thermal rise induced by the acoustic field in the phantom was measured using a gradient echo MR sequence (TR/TE = 25.2/12.4 ms, FOV = $20 \times 20 \text{ cm}^2$, slice thickness = 3 mm). This is applicable due to the linear dependence of the proton resonance frequency (PRF) of the water molecule and temperature:

$$\Delta T = \frac{\Delta\varphi}{C \cdot \gamma \cdot B_0 \cdot TE}, \quad (12)$$

where $C = -0.0091 \text{ PPM } ^\circ\text{C}^{-1}$ is the constant of proportionality, γ is the proton gyromagnetic ratio, B_0 is the magnetic field strength, TE is the echo time and $\Delta\varphi$ is the phase difference between MR phase images measured before and during the heating.

The temperature rise at each focal spot, T_m , was evaluated by taking the maximal ΔT in a region of 7×7 pixels (equivalent to $5.46 \times 5.46 \text{ mm}^2$) around the targeted point. The total temperature elevation is calculated as the sum of the values evaluated for each focal spot, and the pattern uniformity was computed as $u = 1 - \frac{\Delta T_{\max} - \Delta T_{\min}}{\Delta T_{\max} + \Delta T_{\min}}$, where $\Delta T_{\max} = \max_m\{T_m\}$, i.e. the temperature rise in the pixel that exhibited the highest temperature rise, and ΔT_{\min} is defined similarly.

4. Results

4.1. Simulation results

In order to evaluate the relative performance of the different algorithms we used each to compute the phases required to generate multi-focal patterns and computed the resulting efficiency and uniformity. The generated patterns were either symmetric-grid or pseudo-random patterns, situated on a plane parallel to the phased-array plane at a distance of $z = 60 \text{ mm}$. A preliminary subset of simulations showed that all algorithms successfully generate multifocal fields, although with differences in the intensity levels and uniformities between the different foci (examples are shown in figure 2(A)).

The focal spots were found to have similar sizes whatever algorithm is used, which we proceeded to quantify. The focal profiles on the horizontal and vertical axes of a nine foci symmetric grid pattern are very similar and are only slightly wider than the profile of a single focus (figure 1(B)). The mean full-width at half maximum (FWHM) of the foci is

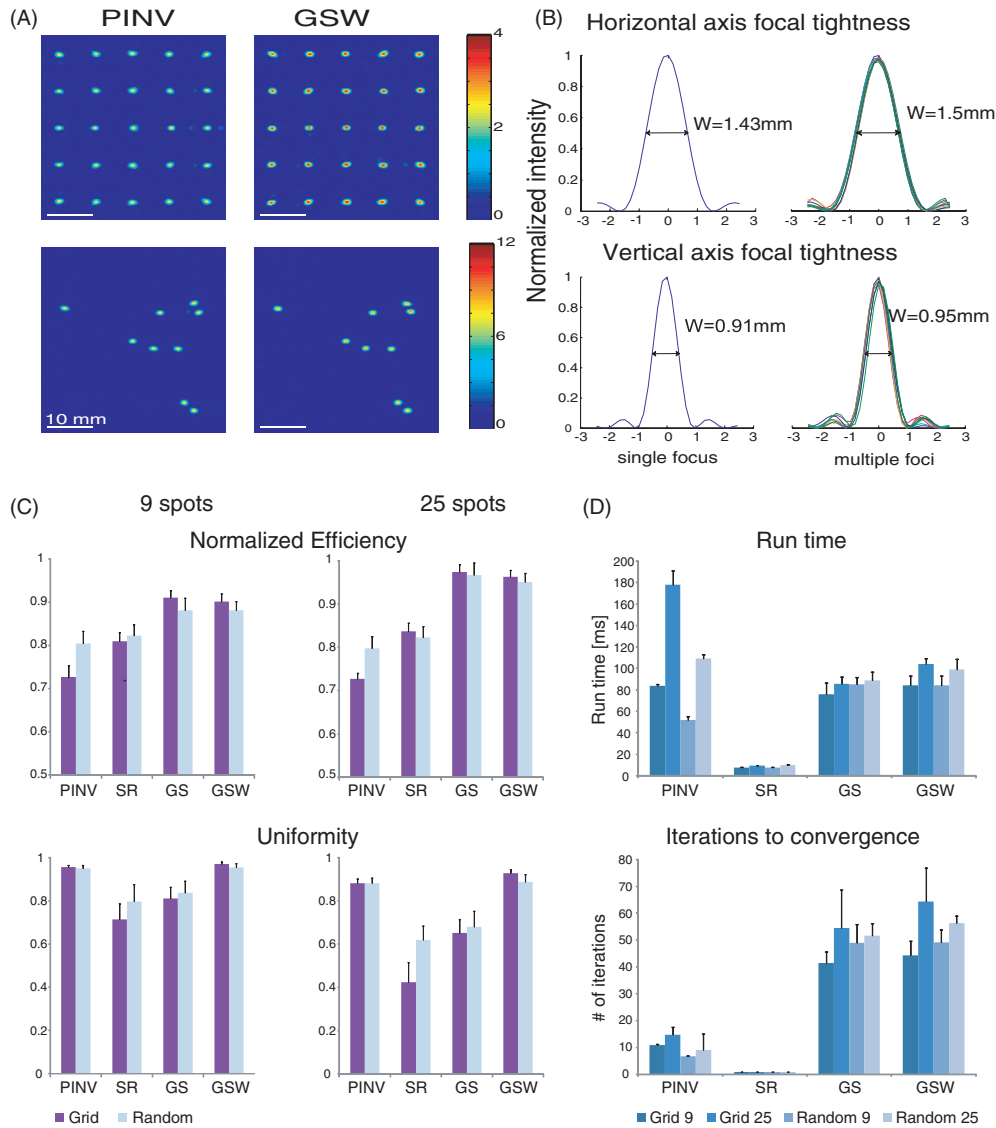


Figure 2. Simulations of multifocal ultrasonic distribution from a 987 element phased array. (A) Ultrasonic intensity maps generated the PINV and GSW algorithms, in arbitrary units of intensity. Top—an axis aligned grid of 25 foci, bottom—a nine spot pseudorandom pattern. Scale bars: 10 mm. (B) The focal tightness of a single generated focus (left) and multiple foci on a nine-foci grid (right), on the horizontal and vertical axes. The tightness of the multiple foci is almost the same as for a single focus as quantified by the full-width half-maximum (FWHM). (C) Comparison of mean efficiencies (top) and uniformities (bottom) measured for sets of 12 pseudorandom and symmetric maps generated by the four algorithms. GSW is the best combination of efficiency and uniformity for both sparseness levels; error bars denote one standard deviation. (D) Evaluation of algorithmic computational effort via the mean run time (top) and mean number of iterations required for convergence (bottom). Error bars denote one standard error of the mean.

0.95 ± 0.02 mm (mean \pm std) on the vertical axis and 1.50 ± 0.03 mm on the horizontal axis, compared to 0.91 and 1.43 mm on the vertical and horizontal axes, respectively, for a single focal spot. The asymmetry of the foci results from the asymmetry of the phased-array aperture, which is wider on the vertical axis, leading to a tighter vertical focus.

A quantitative evaluation was based on two sets of multifocal patterns, with different levels of sparseness. In the first set, nine foci were created within a square of 32×32 mm², and in the second set, 25 foci were created within the same square. The sets were composed of 12 pseudo-random patterns and 12 patterns, which are versions of an axes-aligned grid rotated at an angle of $\theta = \frac{k}{12} \cdot \frac{\pi}{2}$, $k = 0, 1, \dots, 11$. The power delivered to each focus was quantified by summing

the intensity delivered to the FWHM area, approximated by a $1.5 \text{ mm} \times 1.0 \text{ mm}$ rectangular area surrounding the targeted point. In order to avoid overlaps between foci in the pseudorandom set case, we required that the distance between any two targets is at least 1.5 mm.

Comparing the mean efficiencies and uniformities (figure 1(C)), we find that of the CGH algorithms, SR yields the least efficient and uniform patterns, as expected. GS patterns are the most efficient, although only by 1–2% more than GSW patterns, which are the most uniform. Comparing GSW and PINV patterns we find them to have similar uniformities except for the case of the 25 foci grids in which GSW yields patterns which have a mean uniformity larger by 5%. In contrast, GSW patterns have a mean efficiency larger by 17–23% for grid

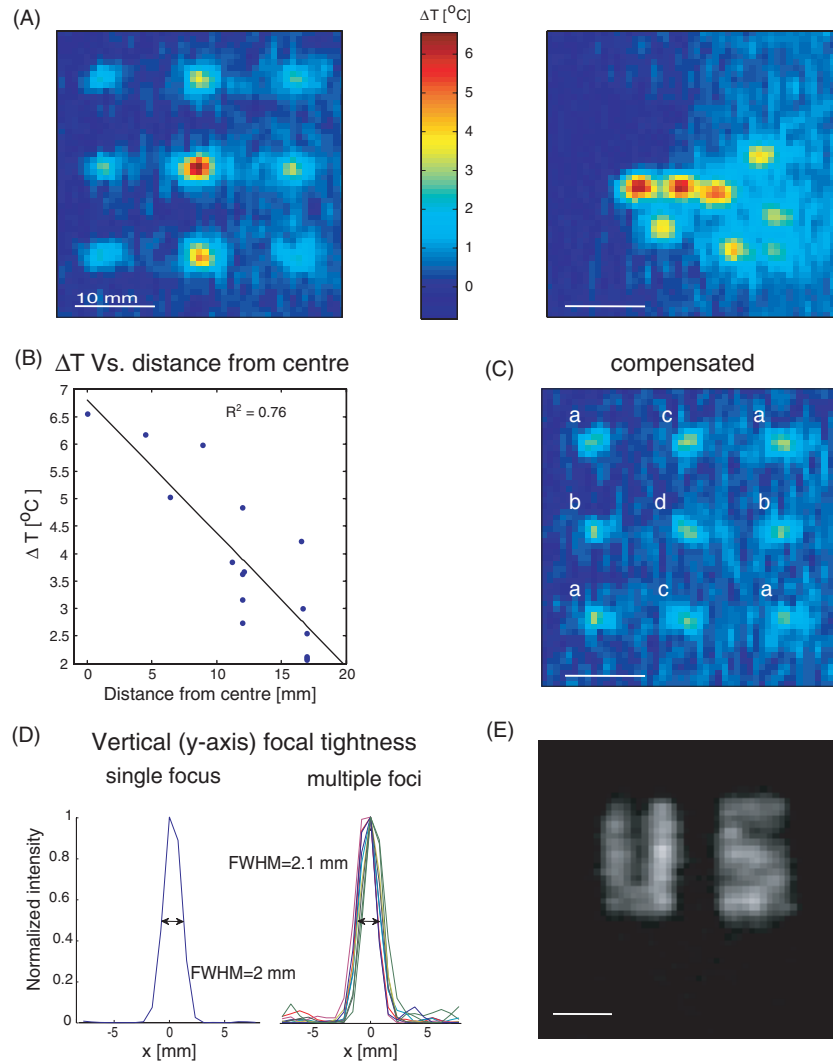


Figure 3. Experimental multifocal ultrasonic distributions from a 987 element phased-array, produced by the GSW algorithm. (A) Temperature elevation maps generated after 13.2 s of sonication. (B) The dependence of the intensity on the transverse distance from the array's centre. (C) The same pattern as in A, generated with compensating weights. The foci marked [a, b, c, d] are weighted by [1, 0.8, 0.74, 0.52], respectively. (D) The focal tightness as quantified for a single central focus (left) and the compensated (right) temperature elevation maps after 13.2 s of sonication. (E) A complex pattern created by 22 focal points. Temperature elevation was measured 19.8 s after the onset of sonication. Scale bars: 10 mm.

patterns and 8–15% for pseudorandom patterns, a difference which increases as the number of foci grows. Overall, the best combination of efficiency and uniformity within the settings of our simulations is given by the GSW algorithm.

To complete the comparison, we evaluated representative computational loads for the different algorithms when implemented in Matlab R2009 A 64-bit, on an HP PC computer equipped with an Intel® Core™ i7 3.07 GHz CPU under the Windows 7 operating system (results shown in figure 2(D)). The least demanding algorithm is the single-step SR, which was also used to initialize GS and GSW. GS (runtimes 76–89 ms) and GSW (runtimes 84–104 ms) generally required a similar mean time per iteration (1.7 ms) and a similar number of iterations to converge (mean difference $\leq 10\%$ except for the dense grid pattern where GSW required 18% more iterations). PINV required on average only 1/5 of the iterations required for GS; however, the average overall runtimes (61–208 ms) were either similar or longer, especially

for the dense grid pattern, because the mean time per iteration for PINV was much longer and also sparsity dependent (7.6 ms and up to 12.1 ms in the dense scenarios). The calculation of the distance matrix entries, d_{mn} , is a short pre-processing step required for all of the algorithms (mean times ranging from 0.6 to 1.1 ms).

4.2. Experimental results

We turn to experimental demonstration of multi-focal field generation through the GSW algorithm, based on the simulations' prediction that it yields the best combination of efficiency and uniformity. The first patterns we generate are the symmetric nine spots grid and a pseudorandom pattern appearing in figure 3(A) (left and right, respectively), generated on a plane parallel to the array plane at a distance of 60 mm. The successful production of the multi-focal field is evident from the temperature elevation maps measured

13.2 s after the onset of ultrasonic irradiation, although the temperature elevation at the foci has low uniformity, quantified as $U = 0.48$ and $U = 0.54$ for the symmetric and pseudorandom maps, respectively. This may be due to the array elements having a radiation profile which deviates too much from the spherical profile implied by the point-source assumption used in our computations. Thus, the focal temperature elevation depends on the distance of the focus from the target plane centre (defined as the point in the target plane that intersects with a vector normal to the array plane and situated at the array centre). This dependence is shown in figure 3(B), which plots the temperature elevations in the foci of the patterns in figure 3(A) against their distance from the centre. (The decrease in temperature elevation appears to be less drastic on the y -axis than the x -axis, which may be due to the array's asymmetric aperture).

It is possible to correct the non-uniformity by using equation (11) to compute the phases required for a non-uniform field, choosing the relative target weights so they compensate for the array's inherent non-uniformity. Figure 3(C) shows a compensated nine spots grid, in which the foci marked [a, b, c, d] are weighted by [1, 0.8, 0.74, 0.52], respectively. This results in greatly improved uniformity, quantified as $U = 0.9$, at the expense of an 11% reduction in the total temperature elevation.

The evaluation of the focal size from our measurements is difficult as we do not measure the actual intensity, and the temperature distribution is smeared due to heat diffusion. Additionally, the pixel size is 0.78 mm, which is almost the focal FWHM predicted by the simulations. However, under these limitations we may evaluate some upper bound to the focal size, which must be smaller in reality. We investigate the focal size in the compensated grid image obtained after 13.2 s of irradiation, finding the FWHM along the vertical and horizontal scales to be 2.2 ± 0.1 mm and 2.4 ± 0.4 mm, respectively (mean \pm std), the former shown in figure 3(D). These values are on a scale similar to the simulated values. The FWHM of a single central focus is 2.1 and 2.2 mm on the vertical and horizontal axes, respectively, slightly smaller than the FWHM in the multi-focal field, in good accordance with the simulations, as well as the vertical/horizontal asymmetry.

Having succeeded in the generation of simple multi-focal patterns, we proceed to produce a more complex pattern with more foci brought closer together. We design a pattern consisting of 22 points, spelling out the letters 'US', and compute the required phases with the GSW algorithm. The resulting temperature elevation after 19.8 s of sonication is displayed in figure 3(E).

5. Discussion

In this paper, we have addressed computationally and experimentally the problem of generating a sparse multi-focal pattern using phase modulations of a phased ultrasonic array, an important first step towards the design and implementation of patterned neuro-stimulators and neuro-modulation systems using ultrasonic waves. Previous studies of multifocal ultrasound, which appeared in the context of hyperthermia,

were based largely on detailed simulations [1–3, 17] without an experimental validation. Lalonde *et al* [18] used the PINV algorithm to compute an array of static phase elements and measured either the intensity distribution sequentially using a hydrophone or the temperature distribution with a thermal camera in a method that required repeated heating before measuring the distribution from each plane. In contrast, we used dynamic phase elements, and by using MR thermometry we were able to obtain a simultaneous view of the resulting intensity distribution.

Although the approximations used in optics when computing CGH do not generally hold for the dimensions, distances and wavelengths used in the ultrasound regime, we have found that CGH algorithms such as GS and the GSW can generally be adapted to this application by using a partial Fresnel approximation. When compared to a key algorithm that was developed for multi-focal ultrasound, the pseudoinverse algorithm, we showed that the GSW provides improved performance for both pseudo-random and symmetric focal distributions.

The simulations we have used were based on a highly simplified and approximate spherical-wave propagation from each (point) transducer. Nevertheless, the experiments we performed verified that they were accurate enough for predicting the generated patterns. However, to fully explain the observed non-uniformity of the efficiency map (figure 3(B)), the point source approximation will probably need to be relaxed, for example by incorporating the elements' spatial pressure distribution into the computation. Alternatively, a pre-calibrated or automatic correction algorithm that assigns compensating weights may be used to compensate for the non-uniformity. Such an algorithm will also help to overcome other issues such as tissue or medium inhomogeneity.

Additional engineering challenges still remain to be addressed before the potential of patterned acousto-stimulation can be fully realized. First, it is interesting and potentially important to examine the extreme near-field behaviour of the computed stimulation patterns (i.e. near the phased-array source). The complex, discontinuous pattern of input phases appears to lead to significant shear strains near the array, and is likely to increase the need for near-field cooling. Also, while our focus here was on sparse stimulation patterns, the generation of non-sparse patterns also needs to be examined in detail, and may require specific speckle-reducing adaptations as it does in the generation of contiguous CGHs [21]. Another issue that must be considered is the passage of transmitted acoustic waves through multiple interfaces with different properties (water and different tissue types) during transcranial sonication. A simple adaptation of the equations in this case can be carried out by replacing d_{mn} with $d'_{mn} = d_{mn}^p \cdot k_{mn}/k$, where d_{mn}^p and k_{mn} are the distance and the average wavenumber of the acoustic path from the n th element to the m th target. Corrections for the related acoustic phase aberrations, caused mainly by the cranium, can be measured [22] and adapted by the multi-focal algorithms to generate efficient and uniform trans-cranial multi-focal patterns.

In upcoming work we are planning to apply the concepts developed here to demonstrate and study experimental

patterned neuro-stimulation, in cortical and sub-cortical structures, building on the major recent progress achieved in single-spot ultrasonic neuro-modulation [4–9]. The potential ability to dynamically and non-invasively control patterned activity in a single structure or in several interacting structures is unique to FUS and holds vast promise both for basic research and for the development of possible applications such as pre-operative diagnostic procedures or neuro-prosthetic devices. It is important to note that the phased-array system we have used for our experimental investigation here is technically similar to another Insightec system (ExAblate 4000) that has been optimized for water-cooled trans-cranial FUS surgery [23], and is already undergoing various clinical trials in animal and human subjects [24, 25]. The acoustic power required for generating neural stimulation (~ 200 mW cm^{-2} , [9]) is two orders of magnitude less than the power delivered trans-cranially in hyperthermia treatments [24] and thus easily within the existing capabilities. The trans-cranial system has a lower operating frequency of 650 kHz and a semi-spherical arrangement over a larger aperture (a diameter of 30 cm compared to 40 mm in the experimental transducer). Our simulations indicated that the multifocal spot size is essentially identical to the single-focus spot volume, which is $2 \times 2 \times 4$ mm³ (FWHM) in the trans-cranial system. The distance to the targets at which the near-field approximations are valid is related to the aperture diameter, yet in the case of a spherical transducer the use of convenient approximations at much shorter distances than the nominal $D^2/4\lambda$ is theoretically valid. Thus, the methods used in the current work will be applicable in experimental trans-cranial multi-focal stimulation, and consequent deviations remain to be empirically investigated. Clearly, other phased-array systems and architectures are also possible in this application, including arrays of micro-transducers [26, 27], which are small enough to potentially be implantable.

Efficient multifocal patterns may also be useful for other FUS applications, such as tissue ablation [28] and permeabilizing of the blood–brain barrier (BBB) [29], in two aspects: time efficiency and the improvement of temporal and spatial acoustic field distributions. Increasing the time efficiency of FUS treatment, which is important especially for tissue ablation [30], is feasible by heating simultaneously multiple targets rather than a single target at a time. Several techniques were proposed to improve spatial and temporal temperature distributions for hyperthermia [31], [3]. Using multifocal patterns, complex spatial distributions of acoustic intensities can be generated under absolute temporal uniformity.

Acknowledgments

The authors acknowledge the financial support of the European Research Council (grant no 211055). They would like to thank Eitan Kimmel and Lior Golan for their helpful advice. They are also grateful for the technical support from Eyal Zadicario and InSightec Ltd, Tirat Carmel, Israel.

References

- [1] Ibbini M S and Cain C A 1989 A field conjugation method for direct synthesis of hyperthermia phases-array heating patterns *IEEE Trans. Ultrason. Ferroelectr. Freq. Control* **36** 3–9
- [2] Ebbini E S and Cain C A 1989 Multiple-focus ultrasound phased-array pattern synthesis: optimal driving-signal distributions for hyperthermia *IEEE Trans. Ultrason. Ferroelectr. Freq. Control* **36** 540–8
- [3] McGough R J, Ebbini E S and Cain C A 1992 Direct computation of ultrasound phased-array driving signals from a specified temperature distribution for hyperthermia *IEEE Trans. Biomed. Eng.* **39** 825–35
- [4] Fry F J, Ades H W and Fry W J 1958 Production of reversible changes in the central nervous system by ultrasound *Science* **127** 83–4
- [5] Gavrilov L R, Tsurulnikov E M and Davies I A 1996 Application of focused ultrasound for the stimulation of neural structures *Ultrasound Med. Biol.* **22** 179–92
- [6] Tyler W J, Tufail Y, Finsterwald M, Tauchmann M L, Olson E J and Majestic C 2008 Remote excitation of neuronal circuits using low-intensity, low-frequency ultrasound *PLoS ONE* **3** e3511
- [7] Muratore R, LaManna J, Szulman E, Kalisz M S A, Lamprecht M, Simon M S M, Yu M S Z, Xu N and Morrison B 2009 Bioeffective ultrasound at very low doses: reversible manipulation of neuronal cell morphology and function *in vitro AIP Conf. Proc.* **1113** 25–9
- [8] Colucci V, Strichartz G, Jolesz F, Vykhodtseva N and Hynynen K 2009 Focused ultrasound effects on nerve action potential *in vitro Ultrasound Med. Biol.* **35** 1737–47
- [9] Tufail Y, Matyushov A, Baldwin N, Tauchmann M L, Georges J, Yoshihiro A, Tillery S I H and Tyler W J 2010 Transcranial pulsed ultrasound stimulates intact brain circuits *Neuron* **66** 681–94
- [10] Golan L and Shoham S 2009 Design and characteristics of holographic neural photo-stimulation systems *J. Neural Eng.* **6** 066004
- [11] Nikolenko V, Watson B O, Araya R, Woodruff A, Peterka D S and Yuste R 2008 SLM microscopy: scanless two-photon imaging and photostimulation using spatial light modulators *Front. Neural Circuits* **2** art 5 1–14
- [12] Lutz C, Otis T S, DeSars V, Charpak S, DiGregorio D A and Emiliani V 2008 Holographic photolysis of caged neurotransmitters *Nat. Methods* **5** 821–7
- [13] Zahid M, Vélez-Fort M, Papagiakoumou E, Ventalon C, Angulo M C and Emiliani V 2010 Holographic photolysis for multiple cell stimulation in mouse hippocampal slices *PLoS ONE* **5** e9431
- [14] Di Leonardo R, Ianni F and Ruocco G 2007 Computer generation of optimal holograms for optical trap arrays *Opt. Express* **15** 1913–22
- [15] Reicherter M, Haist T, Wagemann E U and Tiziani H J 1999 Optical particle trapping with computer-generated holograms written on a liquid-crystal display *Opt. Lett.* **24** 608–10
- [16] Spalding G C, Courtial J D and Di Leonardo R 2008 Holographic optical trapping *Structured Light and its Applications: an Introduction to Phase-Structured Beams and Nanoscale Optical Forces* ed D L Andrews (Amsterdam: Elsevier) pp 139–68
- [17] Gavrilov L R 2003 Use of phased arrays for generation and steering of considerable number of foci *Proc. 13th Session of the Russian Acoustical Society (Moscow)* pp 585–8
- [18] Lalonde R J, Worthington A and Hunt J W 1993 Field conjugate acoustic lenses for ultrasound hyperthermia *IEEE Trans. Ultrason. Ferroelectr. Freq. Control* **40** 592–602

- [19] Goodman J W 2005 *Fourier Optics* 3rd edn (Englewood, CO: Roberts & Company Publishers)
- [20] Angelsen B A J 2000 *Ultrasound Imaging: Waves, Signals and Signal Processing* vol 1 (Trondheim: Emantec AS)
- [21] Golan L and Shoham S 2009 Speckle elimination using shift-averaging in high-rate holographic projection *Opt. Express* **17** 1330–9
- [22] Hertzberg Y, Volovick A, Zur Y, Medan Y, Vitek S and Navon G 2010 Ultrasound focusing using magnetic resonance acoustic radiation force imaging: application to ultrasound transcranial therapy *Med. Phys.* **37** 2943–51
- [23] Hynynen K, McDannold N, Clement G, Jolesz F A, Zadicario E, Killiany R, Moore T and Rosen D 2006 Pre-clinical testing of a phased array ultrasound system for MRI-guided noninvasive surgery of the brain—a primate study *Eur. J. Radiol.* **59** 149–56
- [24] Cohen Z R, Zaubermann J, Harnof S, Mardor Y, Nass D, Zadicario E, Hananel A, Castel D, Faibel M and Ram Z 2007 Magnetic resonance imaging-guided focused ultrasound for thermal ablation in the brain: a feasibility study in a swine model *Neurosurgery* **60** 593–600
- [25] Martin E, Jeanmonod D, Morel A, Zadicario E and Werner B 2009 High-intensity focused ultrasound for noninvasive functional neurosurgery *Ann. Neurol.* **66** 858–61
- [26] Wygant I O, Zhuang X, Yeh D T, Vaithilingam S, Nikoozadeh A, Oralkan O, Ergun A S, Karaman M and Khuri-Yakub B T 2005 An endoscopic imaging system based on a two-dimensional CMUT array: real-time imaging results *Proc. IEEE Ultrasonics Symp.* **2** 792–5
- [27] Wong S H, Watkins R D, Kupnik M, Pauly K B and Khuri-Yakub B T 2008 Feasibility of MR-temperature mapping of ultrasonic heating from a CMUT *IEEE Trans. Ultrason. Ferroelectr. Freq. Control* **55** 811–8
- [28] Jolesz F A 2009 MRI-guided focused ultrasound surgery *Annu. Rev. Med.* **60** 417–30
- [29] Hynynen K, McDannold N, Vykhodtseva N and Jolesz F A 2001 Noninvasive MR imaging-guided focal opening of the blood-brain barrier in rabbits *Radiology* **220** 640–6
- [30] Fan X and Hynynen K 1996 Ultrasound surgery using multiple sonications—treatment time considerations *Ultrasound Med. Biol.* **22** 471–82
- [31] Mougnot C, Salomir R, Palussiere J, Grenier N and Moonen C T W 2004 Automatic spatial and temporal temperature control for MR-guided focused ultrasound using fast 3D MR thermometry and multispiral trajectory of the focal point *Magn. Reson. Med.* **52** 1005–15